A programmable modular lattice metamaterial with multiple deformations

Hao Chen, Yongtao Yao, Yanju Liu, Jinsong Leng & Wenfeng Bian

Published online: 29 Aug 2023.

Submit your article to this journal ☑

View related articles ☑

View Crossmark data ☑

Taylor & Francis
Taylor & Francis Group

Check for updates

ORIGINAL ARTICLE

A programmable modular lattice metamaterial with multiple deformations

Hao Chen[a], Yongtao Yao[a], Yanju Liu[a], Jinsong Leng[a] (iD), and Wenfeng Bian[b]

[a]Centre for Composite Materials and Structures, Harbin Institute of Technology (HIT), Harbin, People's Republic of China; [b]Department of Civil Engineering, Harbin Institute of Technology (HIT), Weihai, People's Republic of China

ABSTRACT

This paper describes a class of lattice metamaterials with tunable mechanical properties controlled by the material modulus and structural parameters of the cellular units. The deformation shapes can also be changed by external control. We have developed 3D printed quadrilateral cellular TPU units with specially shaped edge walls. A simplified mechanical model of the different cell deformation processes is established and verified by numerical simulations and experiments. On this basis, by tessellating and matching these transformations together, we create assembly grids with adjustable stiffness and deformation shapes controlled by thermal and displacement constraints.

1. Introduction

The demand for materials with excellent functions and properties is increasing with the progress of modern engineering technologies, and there has been a growing interest in designing tunable material systems that allow deformable shapes/structures [1]. Among these, mechanical metamaterials have a wider range of applications due to their unusual mechanical properties derived from their special microstructural geometry than classical materials of the same material composition [2–5]. Metamaterials are often artificial structural composites made up of periodically arranged cells that not only enhance the properties of the constituent materials, but also have different functions and unusual properties [6–7]. By combining lattice structures with the introduction of mechanical metamaterials through rationally design, the metamaterial structures not only retain the characteristics of the lattice structures, such as excellent strength, energy absorption, thermal insulation, noise suppression and light weight characteristics, but also obtain new and unique mechanical properties, such as anisotropy, negative stiffness and negative Poisson's ratio [8–16].

At this point, the mechanical properties of the structures depend not only on the structural materials themselves, but also on the design and deformation patterns of their microstructures, and can be customized through appropriate microstructure design and arrangement [17–22]. For example, Gao et al. designed a new class of new 3D lattice structures that are capable of offering Poisson's ratio from positive to negative in a wide range along the three principal axes [23]. Fan et al. proposed novel two-phase hybrid strategies based on different types and numbers of thin-plate cubic cells, and quasi-static compression experiments and finite element numerical simulations were performed to

investigate their energy absorption characteristics and deformation mechanisms [24]. Ou et al. developed four cellular-based material structure units composed of rigid plates and elastic/rotary hinges, so that different compositions of these units lead to a variety of tunable shape-changing possibilities, such as uniform scaling, shearing, bending and rotating [25]. Huang et al. proposed a novel dual architecture phase lattice structure consisting with hard and soft phases [26]. Zhang et al. proposed a pixel design method for mechanical metamaterials arrangement based on topology optimization and obtained two different objectives: the maximum stiffness (MS) and the maximum stiffness with minimum Poisson's ratio (MSMP) by this method [27]. Thus, programmable mechanical metamaterials have the potential to be widely used in aerodynamics, modern heat-transfer applications, soft robotics, flexible electronics, aerospace engineering, biomedical engineering and other fields [28–37].

From the literature, most of the reported lattice metamaterials are arranged in combinations around homogeneous or heterogeneous units to achieve specific functions. Among these, the ability to freely assemble with modular design is a relatively recent breakthrough. In addition, the use of differentiated temperature field distributions to control the mechanical properties of lattice structures is scarcely mentioned in the literature.

In this paper, we propose a mechanical metamaterial structure based on flexible polymeric materials whose modulus varies with temperature, which is composed of several unit cells that can be assembled in a modular way, and exhibit programmable responses, including stiffness and deformation patterns, through a variety of external controls, including temperature and displacement constraints. To

---

achieve this goal, a commercial polymeric material (thermoplastic polyurethane, TPU) is selected to fabricate quadrilateral cellular units with specially shaped edge walls by 3D printing. Those units can be assembled modularly and programmed to transform into different shapes including concave, convex and shear deformation under different temperature and displacement constraints when subjected to unidirectional compression. In this paper, simplified mechanical models of different deformation processes of cellular elements are established. The relationships between mechanical properties of cells or their assembly structures, modulus of material and structural parameters are discussed, and are verified by numerical simulations and experiments.

2. Designs and mechanical models

2.1. Designs

Consider the quadrilateral cellular unit shown in Figure 1(a), which can be divided into three regions ①②③ as shown in Figure 1(b).

For region ①, it consists of two sheet structures mirroring each other as shown in Figure 1(c), which can be regarded as being formed from the geometric shape of Figure 1(d) after equal-width stretching width b. Its length is l_0, the upper surface has a parabolic curvature and an arch height g, and the lower surface is flat and there is a slot with a top width a_1, a bottom width a_2, and a depth f. At the slotted position, the thickness of the thinnest point of the structure is z. This region is composed of flexible material and is the main region where deformation occurs in the lattice cell, and the slotted area can be subjected to thermal constraints to control the deformation pattern of the lattice cell.

For region ②, it is composed of rigid material, distributed at the four corners of the lattice cell and protruding slightly in the width direction. The displacement constraints can be

applied at these protruding locations to control the deformation pattern of the lattice cell.

For region ③, it serves to transfer the displacement and stress, and has no special requirements on the material and shape.

2.2. Determination of shape deformation patterns

For the case where displacement constraint exists, the quadrilateral grid cell is subjected to the compressive displacement U_x. When the displacement of each prominent corner points (region ②) in the y-direction is constrained and no rotation occurs, as shown in Figure 2(a), the deformation of the structure is equivalent to the compression displacement acting directly and uniformly on region ③ without considering the deformation of region ③. At this time, region ① can be regarded as being fixed-pinned, and the deformation will be also deformed along the y-axis in the positive or negative direction due to its curvature (including arches and slots). This corresponds to one of the convex/concave deformations of the grid cell, as shown in Figure 2(b). With a rational geometric design, it is possible to separate the two states of deformation by applying a temperature constraint at the slotted area in region ①.

When no temperature constraint is applied, as shown in Figure 2(c), let the neutral axis of region ① lie at the geometric center, which is separated from the inner boundary of the external cube of the structure by e_0. Assume that there exists an external center line such that the external cube has an equal chance of deforming in both directions after compression, and let it lie at the geometric center of the external cube, which is separated from the inner boundary of the external cube of the structure by e. Obviously, e does not vary with position and $e = (f + z + g)/2$.

When the neutral axis is not lower than the external geometric center line at any position, as $e_0 \geq e$, the structure
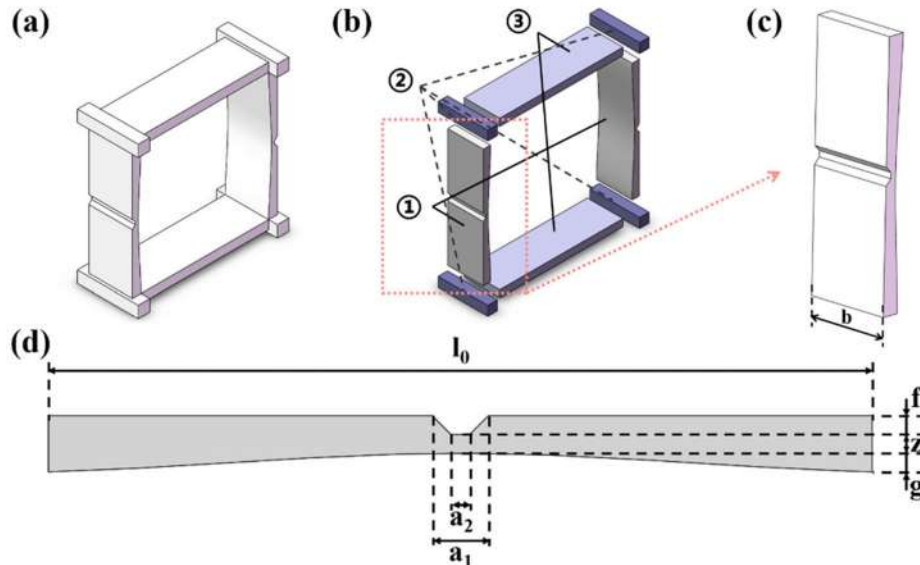

Figure 1. The design of quadrilateral cellular units. (a) A quadrilateral cell. (b) Exploded view of the quadrilateral cell which can be divided into three regions: ①Flexible sheets, ②Prominent corner points, ③Sheets to transfer the displacement and stress. (c) A flexible sheet structure with an arch and a slot in region ①. (d) The geometric parameters of a flexible sheet in region ①.
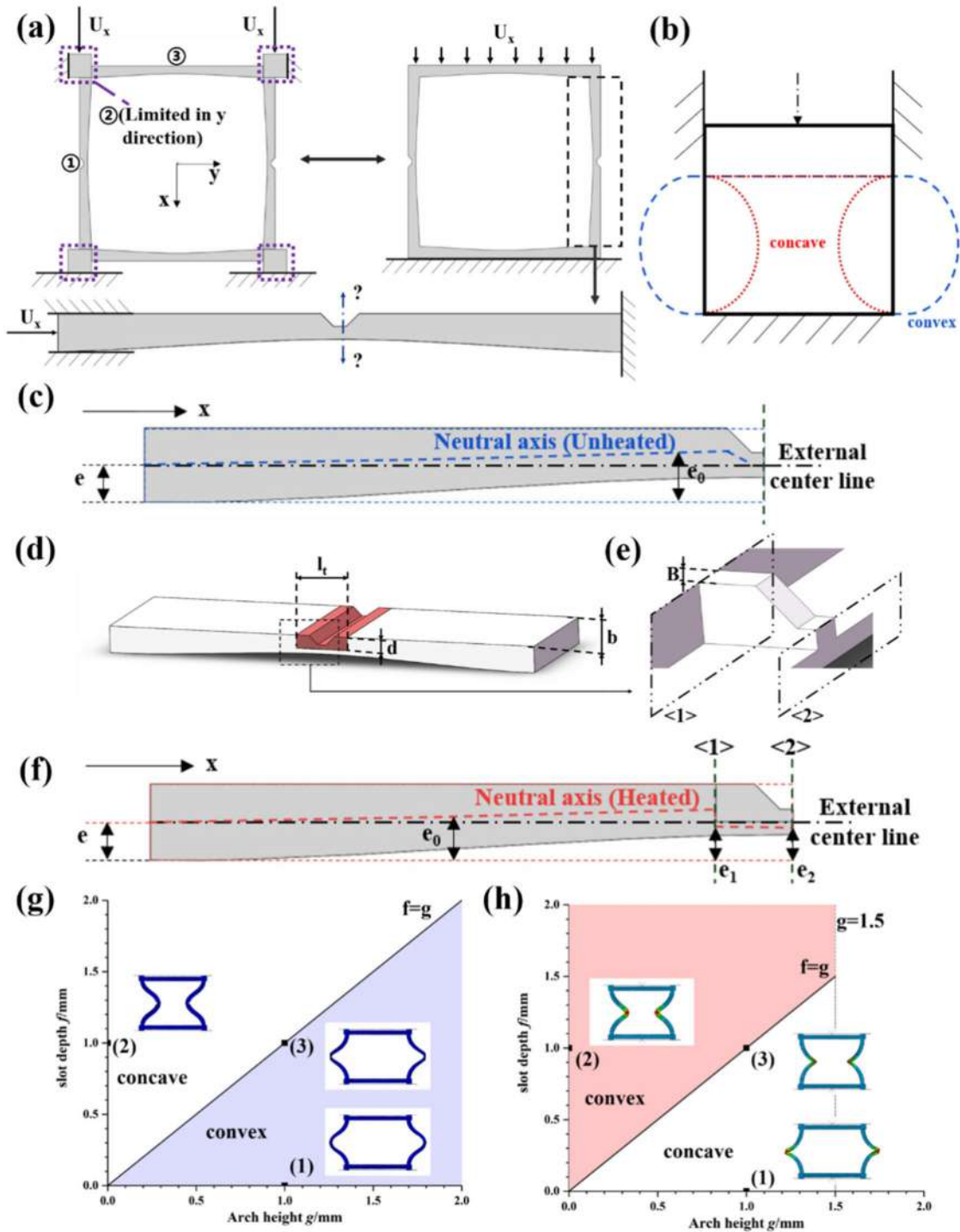
Figure 2. (a) Constrained prominent corner points at compressive displacement. (b) The grid cell deforms convexly or concavely, depending on the constraints. (c) The neutral axis and the external center line of region ① at low temperature, a half cross-section is shown. (d) The heated domain at the slot. (e) Equivalent T-shaped equivalent cantilever model of the heated domain. (f) The neutral axis and the external center line of region ① when heated, a half cross-section is shown. (g) Structural deformation obtained by finite element simulation at low temperature of flexible edge walls and (h) when heated at slots. There are three extreme states: (1) without slotting, (2) without arching, and (3) at $f = g$.

tends to deform more in the direction of the neutral axis protrusion, i.e. the slot protrudes to the outside and the structure undergoes convex deformation. Then there is:

$$b \leq g \tag{1}$$

When a temperature constraint is applied, as shown in Figure 2(d), the modulus of the material at heated domain changes from E_1 at low temperature to E_2 at high temperature. The heated domain can be viewed as a region of length l_t and thickness d. Its mechanical model is equivalent to the T-shaped equivalent cantilever model shown in Figure 2(e) [38], where the modulus at any position is E_1 and the shape of the unheated position remains the same, but the width of the heated domain becomes $B = \frac{E_2}{E_1} b$. As shown in Figure 2(e–f), the neutral axis of the model has two limiting points to the position: the heated domain

boundary <1>, and the central symmetry axis <2>. The distance between the neutral axis and the inner boundary of the external cube is:

$$e_i = \frac{E_1 h_0^2 - E_2 h_i^2}{2(E_1 h_1 + E_2 h_2)} + h_0, \quad i = 1, 2 \tag{2}$$

where $h_0 = f + z - d$, $h_1 = d$, $h_2 = d - f$.

When the neutral axis is not higher than the external geometric center line at any position, the structure tends to deform more in the direction of the neutral axis protrusion, i.e. the slot protrudes inward and the structure undergoes concave deformation. Then there is $e_i \leq e$, the solution is:

$$\begin{cases} g \leq d = f + z - \Delta d \approx f + z \\ g \leq f \end{cases} \tag{3}$$

According to Equations (1) and (3), the range of deformation states of the grid cell at different temperatures and geometrical parameters can be established. The flexible edge walls in region ① have three extreme states: (1) without slotting, (2) without arching, and (3) at $f = g$. At $f + z + g = 3mm$, the structural deformation obtained by finite element simulation against the theoretical deformation states is shown in Figure 2(g–h). It can be concluded that the structure undergoes only one kind of deformation when there is no slotting or arching, regardless of whether the temperature is applied or not, and when $f = g$, the temperature plays a conversion role in the convex/concave deformation of the structure. Essentially, the local reduction of modulus in the heated domain leads to the preferential deformation of this
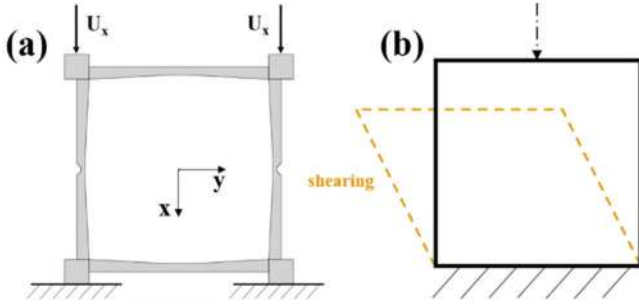
region, which then drives the deformation of the unheated domain.

Therefore, the deformation state of the structure can be controlled by adjusting geometric parameters and temperature, and the closer the geometric parameters are to $f = g$, the more obvious the shape changes brought by temperature.

When boundary corners are not constrained by displacement, as shown in Figure 3(a,b), the structure tends to undergo shear deformation under compression, and flexible sheets at regional ① rarely bear loads, which will lead to the reduction of the compression force, and it depends more on the action between the corner points and flexible sheets than on the flexible sheets themselves.

2.3. Mechanical models for deformation

For the symmetrical half of the flexible sheets at region ①, it can also be divided into three parts, named, <i>, <j>, <k>, respectively corresponding to the main body of the structure (non-heated domain), slotted slope and slot (heated domain), as shown in Figure 4(a). Let the coordinate along the length direction be c and the end be the origin, then the coordinates of each region and its demarcation point are known. The height of the arch of parabolic shape at any point is:

$$\Delta g(c) = \frac{4g}{l_0^2} c^2 \tag{4}$$

2.3.1. Basic assumptions

Assuming that the flexible sheet at region ① has a sinusoidal deflection curve after deformation:

$$y(x) = \frac{U_y}{2}\left[1 - \cos\left(\frac{2\pi x}{l_c}\right)\right] \tag{5}$$

where U_y is the maximum deflection, l_c is the length after deformation, and x is the coordinate along the length direction. Make sure that the coordinate c before deformation and x after deformation are two sets of coordinates. and the full length of the deflection curve is:

$$l[y(x)] = \frac{U_y^2 \pi^2}{4l_c} + l_c \tag{6}$$

so that, the compression displacement $U_x = l_0 - l_c$.

Figure 3. (a) Unconstrained prominent corner points at compressive displacement. (b) The structure tends to undergo shear deformation under compression.
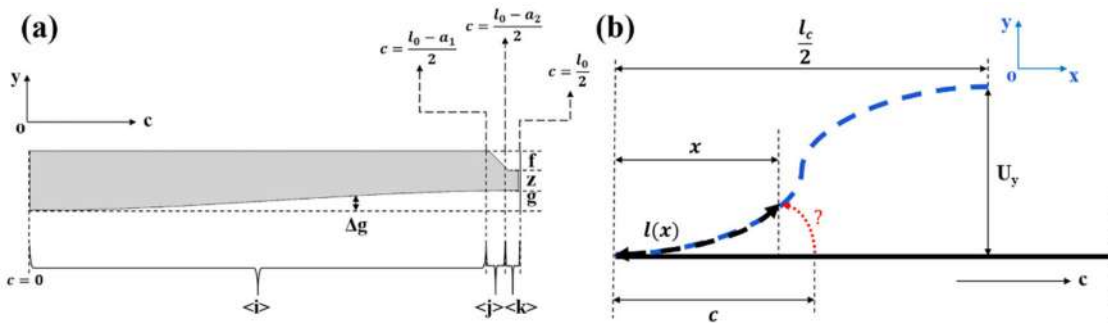

Figure 4. (a) The symmetrical half of the flexible sheets at region ① can be divided into three parts: the main body of the structure (non-heated domain), <j> slotted slope (heated domain), <k> slot (heated domain). The location of the bounding coordinates for each part is given. (b) The flexible sheet is deformed from the original shape (solid line) to a surface with deflection (dashed line), the coordinate c before deformation and x after deformation are two sets of coordinates.

There is a relationship between the compression force F_N and the compression energy U_c and bending potential energy U_b of the structure:

$$F_N = \frac{\partial}{\partial U_y}(U_c + U_b) \tag{7}$$

assuming that there is so little compression energy U_c that $U_c \approx 0$. In other words, that is, the full length of the deflection curve does not change during the deformation, $l[y(x)] \equiv l_0$. So that:

$$U_y = \sqrt{\frac{4l_cU_x}{\pi^2}} \tag{8}$$

Considering that the edge walls are variable section structures, the bending potential energy U_b without temperature constraints should be written as:

$$U_b = \int_0^{l_c} \frac{E_1}{2}I(c)\ddot{y}^2(x)dx = E_1\int_0^{\frac{l_c}{2}} \frac{I}{(c)}\ddot{y}^2(x)dx,$$

$$I(c) = I[l(x)] = \frac{b}{12}h(c)^3,$$

$$h(c) = \begin{cases} f + z + g - \frac{4g}{l_0^2}c^2, & <\text{i}> \\ f + z + g - \frac{4g}{l_0^2}c^2 - \frac{2c - l_0 + a_1}{a_1 - a_2}f, & <\text{j}> \\ f + z + g - \frac{4g}{l_0^2}c^2 - f, & <\text{k}> \end{cases}$$

$$c = c(x) = l(x) \tag{9}$$

where $l(x)$ is the length of the deflection curve from any point x to the origin after deformation.

2.3.2. The relations between coordinate c and x
For the coordinate c before deformation, there is:

$$c = l(x) = \int_0^x \sqrt{1 + [\dot{y}(x)]^2}dx \tag{10}$$

and Equation (10) is an elliptic integral that can be approximated by Taylor expansion as:

$$c \approx \left[\left(\frac{U_y\pi}{2l_c}\right)^2 + 1\right]x - \frac{l_c}{16\pi}\left(\frac{U_y\pi}{l_c}\right)^2\sin\left(\frac{4\pi x}{l_c}\right) \tag{11}$$

$$= k_1 \cdot x - k_2\sin(k_3x)$$

where $k_1 = k_1(U_y) \geq 0$, $k_2 = k_2(U_y) \geq 0$.

2.3.3. Simplification of models
Based on Equations (5), (9) and (11), The bending potential energy U_b without temperature constraints can be written as:

$$U_b = \frac{E_1 b\pi^4 U_y^2}{6l_c^4}f(x, U_y)$$

$$f(x, U_y) = \int_0^{\frac{l_0 - a_1}{2l_0}l_c}(n_{01} - n_1c^2)^3\left(1 + \cos\frac{4\pi}{l_c}x\right)dx$$

$$+ \int_{\frac{l_0 - a_1}{2l_0}l_c}^{\frac{l_0 - a_2}{2l_0}l_c}(n_{02} - n_1c^2 - n_2c)^3\left(1 + \cos\frac{4\pi}{l_c}x\right)dx \tag{12}$$

$$+ \int_{\frac{l_0 - a_2}{2l_0}l_c}^{\frac{l_c}{2}}(n_{03} - n_1c^2)^3\left(1 + \cos\frac{4\pi}{l_c}x\right)dx$$

then the compression force F_N can be written as:

$$F_N = \frac{\partial U_b(x, U_y)}{\partial U_y}$$
$$= 2kU_yf(x, U_y) + kU_y^2\dot{f}(x, U_y) \tag{13}$$

where n_{01}, n_{02}, n_{03}, n_1, n_2, $k \geq 0$.

As $x \gg 1$, all sine terms can be considered as extremely small in Equations (11) and (12). So:

$$f(x, U_y) \approx$$
$$\int_0^{\frac{l_0 - a_1}{2l_0}l_c} m_1h(c)^3dx + \int_{\frac{l_0 - a_1}{2l_0}l_c}^{\frac{l_0 - a_2}{2l_0}l_c} m_2h(c)^3dx \tag{14}$$
$$+ \int_{\frac{l_0 - a_2}{2l_0}l_c}^{\frac{l_c}{2}} m_3h(c)^3dx$$

where $0 \leq m_1, m_2, m_3 \leq 1, h(c) \propto x^2$.

2.3.4. Approximate models and conclusions
Equation (14) shows that the mechanical properties of the edge walls as variable section structures can be treated as a superposition of individual roles, which are the three parts named, $<\text{i}>$, $<\text{j}>$, $<\text{k}>$ (Figure 4(a)) at the flexible sheets at region ① (Figures 1(b) and 2(a)), for the same structural parameters and boundaries are shared between each of the parts and each of the integral terms in Equation (14). Thus there is an approximate model:

$$f(x, U_y) \approx \sum H_i(x^7)\,|_{c_{i,\min}}^{c_{i,\max}}$$
$$\approx \sum \left(\frac{h_{i,\max}^3}{4} + \frac{3h_{i,\min}^3}{4}\right) \cdot n_x, \tag{15}$$
$$i = <\text{i}>, <\text{j}>, <\text{k}>$$

where $H_i(x^7)$ is a seventh degree polynomial with respect to x, n_x is a length parameter of coordinate x, and is proportional to the length of each part, $c_{i,\max}$ and $c_{i,\min}$ are the boundaries of all parts ($<\text{i}>$, $<\text{j}>$, $<\text{k}>$), and $h_{i,\max}$ and $h_{i,\min}$ are the maximum and minimum values of thickness h in each of the parts. Thus, the compression energy U_c and the compression force F_N can be solved when no temperature constraints are loaded.

For the case of temperature constraints, the modulus of the material and the sections of the structure both varies with location. Thus there is an approximate model:

$$U_b = \frac{b\pi^4 U_y^2}{6l_c^4}f(x, U_y, E)$$
$$f(x, U_y, E) \approx \sum E_i\left(\frac{h_{i,\max}^3}{4} + \frac{3h_{i,\min}^3}{4}\right) \cdot n_{x,l_t} \tag{16}$$
$$i = <\text{i}>, <\text{j}>, <\text{k}>$$

where E_i is the modulus of material for each part, and n_{x,l_t} is a length parameter of coordinate x and width of heated domain l_t. Therefore, the flexible sheet with variable cross-section in region ① can be regarded as a weighted superposition of several different sets of constant cross-section but equal length sheets, which is still valid for local modulus inhomogeneities caused by temperature, and the preferentially deformed heated domains and less-deformed unheated domains are independent of each other at initial pressure.

It should be noted that this model is only an approximate model for compression in region ①. Though region ① is the most critical region in the deformation of the structure, the deformation of regions ② and ③ may also be taken into account. After considering the deformation of regions ② and ③, the deformation of region ① may not be idealized, for example, the deflection curve may not be sinusoidal. In addition, the model only provides a first order approximation to the definite integral equation, and the shape of the heated region is also an idealized approximation.

We speculate that the theoretical model is more suitable in the following conditions. The shear and out-of-plane deformation are not considered, the compression displacement is of the same order of magnitude as the structural dimensions, regions ② and ③ are approximately free of deformation, and the structure is well heated.

3. Results and discussion

3.1. Single unit

Figure 5(a) shows the deformation under compression of a single unit whose flexible edge walls are the same as those in Figure 2(g) (3), by comparing simulation and experiment results. Friction exists between the unit and experimental platform as a displacement constraint. For one of the states which has no temperature constraints, at room temperature the unit deforms convex. And in other case, after a temperature constraint at the slots of region ① (Figure 2(a,d)) by external heating films (Figure 7(d)), the heated domains deform easier so that the unit deforms concave as opposed to the deformation in its no temperature constraints. Such deform states are consistent with theoretical expectations.

Figure 5(b–e) shows the force–strain and equivalent stiffness–strain response at two states which are predicted by theories and FE simulations, and are compared with experiment results. For both of the states, with the increasing of strain, the compression force increases and gradually converges to a stable value, while the equivalent stiffness decreases and gradually converges to zero. The force and equivalent stiffness at no constraints is reasonably higher than those in temperature-constraint state. This is the result of the local modulus reduction in the heated domain.

The results show some differences in the stiffness of structure obtained by analytical method, FE simulation and experiments, especially when the compression strain is less than $0.05\,\mathrm{mm\cdot mm^{-1}}$. We speculate on the four reasons for this discrepancy.

Firstly, the theoretical model is an approximate model with errors when the compression strain is relatively small.

Secondly, the theoretical model does not take into account the deformation of regions ② and ③.

Thirdly, the friction forces are not taken into account in the theoretical model and simulation. The pressure forces offset against the friction forces among the assembled parts, resulting in low results at lower compression strains.

Finally, the friction forces between the sliding rails and the assembly are not included in theoretical and simulation results, which exist in the experiment. The sliding rails are not perfectly straight, so the frictional forces at the corner points change due to compression displacement, causing the pressure and equivalent stiffness curves to fluctuate in the experimental results.

However, there is a same trend in analytical, FE simulation and experiment results, that the compression force increases by strain and gradually converges to a same stable value, the equivalent stiffness decreases by strain and gradually converges to zero. In this case, it can be considered that the theoretical model to be considered reasonably convincing.

3.2. Assembly lattices

Figure 6(a) shows the deformation under compression of the assembly structure, which is composed by 3×3 units as above-mentioned, by simulation and experiment. The units assemble each other by prominent corner points, and all of them can be freely disassembled as well, as shown in Figure 7(a). The temperature constraints are provided by heating films (Figure 7(d)), and the displacement constraints are provided by external sliding rails, which can limit the corner points at each line to move only in the compress direction. Without sliding rails, corner points can move in the direction perpendicular to the compression as well.

The deformations of the assembly structure shown by simulations and experiments in different constraints are almost the same. Each unit of the assembly shows the same shape-transform pattern as in the case of individual compression of the unit. The temperature constraints locally affect only the heated cellular units and are independent of the unheated cells. Depending on the type of constraint, cells in the assembly shows concave, convex and shearing deformation, which are consistent with theoretical expectations.

Figure 6(b,c) show the force–strain and equivalent stiffness–strain response at displacement constraints, so that units deform concave/convex due to temperature. For the case without temperature constraints, as in Figure 6(b,c), the assembly is all at room temperature, and it can be seen that the force and equivalent stiffness of the assembly follow the same trend with strain as in the case of a single unit (the FE simulated values no longer converge after the contact of the structure occurs). The equivalent stiffness of the structure is easily known to be three times that of a single unit according to the parallel series equation, as predicted by the theory in Figure 6(b,c).

For the case of simultaneous action of temperature and displacement constraints, as in Figure 6(d,e), the modulus of the structure is significantly lower than that at room temperature, due to the low local modulus of the heated units, which play important roles in deform after compression, while the unheated units have almost no deformation. So the equivalent modulus of the structure is close to the modulus of the whole area composed of the heated units, while the correlation with the unheated units is low.

For the case of no displacement constraints, as shown in Figure 6(f), the sliding rails are removed at this point, the corner points can move perpendicular to the compression direction, and the unit changes from compression-bending
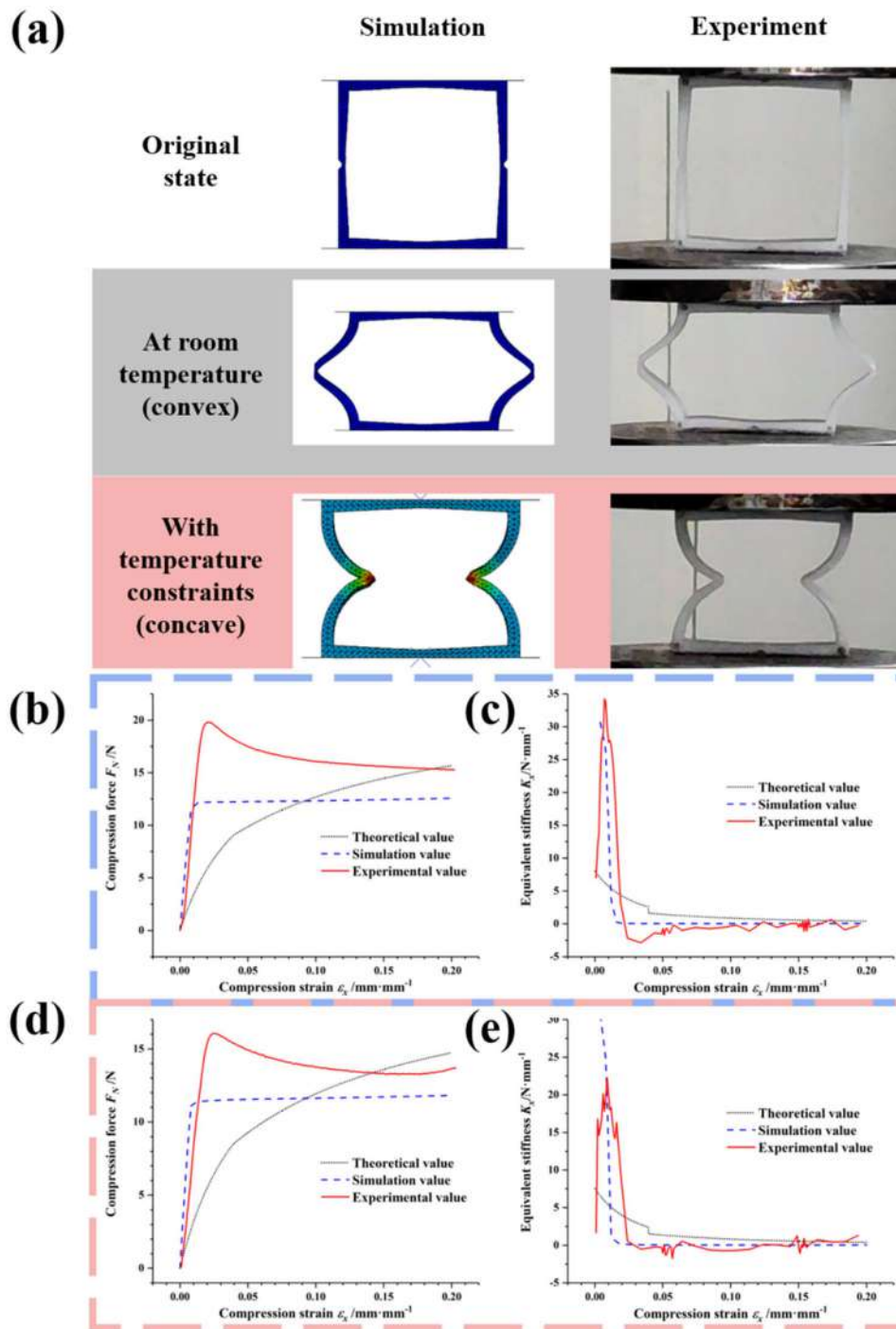
Figure 5. (a) Deformation under compression of a single unit by simulation and experiment. Friction exists between the unit and the experimental platform as a displacement constraint. The original state, the state at room temperature and the state with temperature constraints at the slotted area are shown. (b) Force–strain response at room temperature, (c) Equivalent stiffness–strain response at room temperature, (d) Force–strain response with temperature constraints, (e) Equivalent stiffness–strain response with temperature constraints are predicted by theories and FE simulations, and measured in experiments.

deformation to compression-shear deformation. According to the experimental results, the compression force of the structure is reduced at the same temperature compared to the displacement constraints. This is consistent with the results obtained from theory.

3.3. Discussion

In the results of the theory, FE simulations and experiments, the trends of compression force and equivalent modulus

with strain are almost the same. The units or the assembly share the same deformation patterns controlled by temperature and displacement constraints, although there are some differences between them due to the simplification of the theoretical model, the choice of simulation parameters and elements, and experimental factors. Moreover, the deformation of each unit of the assembly, the compression force and the equivalent modulus of the unit itself are independent of each other, and are not influenced by other units. Therefore, it can be assumed that the mechanical properties
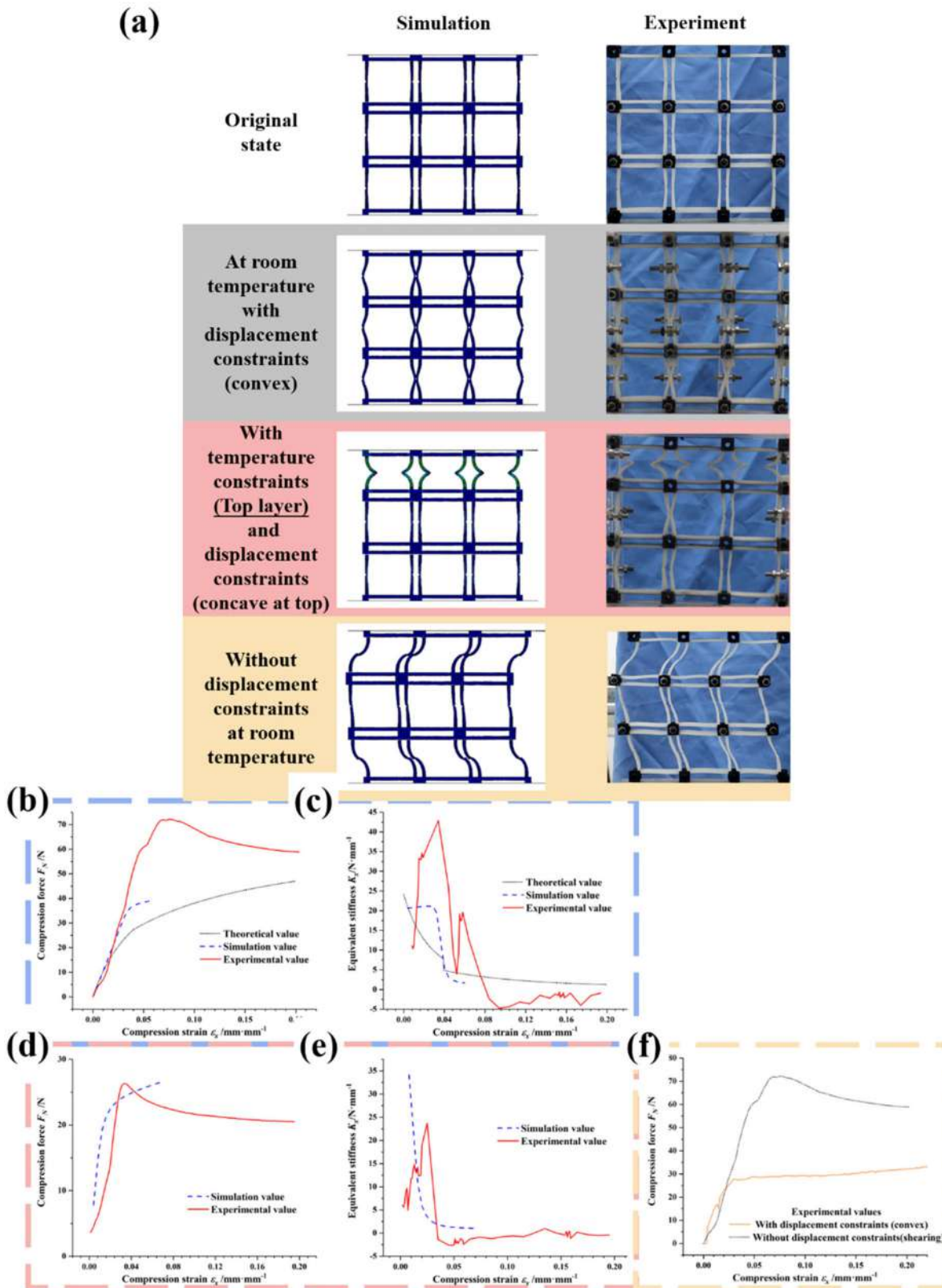
Figure 6. Experiment methods. (a) 3D-printed nylon prominent corner points and TPU lattices linked by metal pins. (b) Calibration lines for the outer boundary (straight) and the inner boundary (parabolic). The units should be placed here for calibration after an experiment was done. To reinforce the units, metal sheets should be glue-bonded to the surface. (c) External sliding rails that provide displacement constraints, and the bolts inside the corner points can slide up and down. (d) External heating films which provide temperature constraints should held in slots by clamps.

of the assembly and the way the shape changes can be designed programmatically according to each detachable individual unit.

One of the potential applications of this structure is encoded display. Figure 8(a). shows a cross-shaped five-unit assembly structure, whose prominent corner points of the
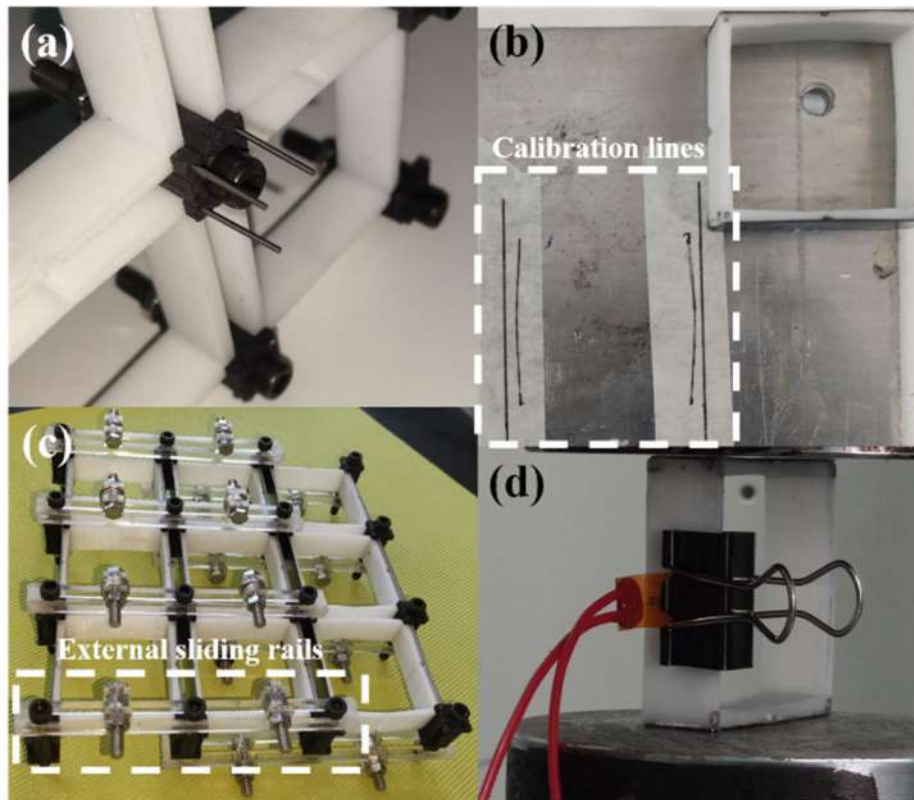
Figure 7. (a) Deformation under compression of assembly lattices by simulation and experiment. The original state, the state at room temperature with displacement constraints, the state with temperature constraints at the top layer and with displacement constraints, and the state without displacement constraints at the slotted area are shown. (b) Force–strain response, (c) Equivalent stiffness–strain response at room temperature with displacement constraints are predicted by theories and FE simulations, and measured in experiments. (d) Force–strain response, (e) Equivalent stiffness–strain response with temperature and displacement constraints are predicted by FE simulations, and measured in experiments (the FE simulated values no longer converge after the contact of the structure occurs). (f) Comparison of the force–strain responses measured in experiments at room temperature for the states with and without displacement constraints.
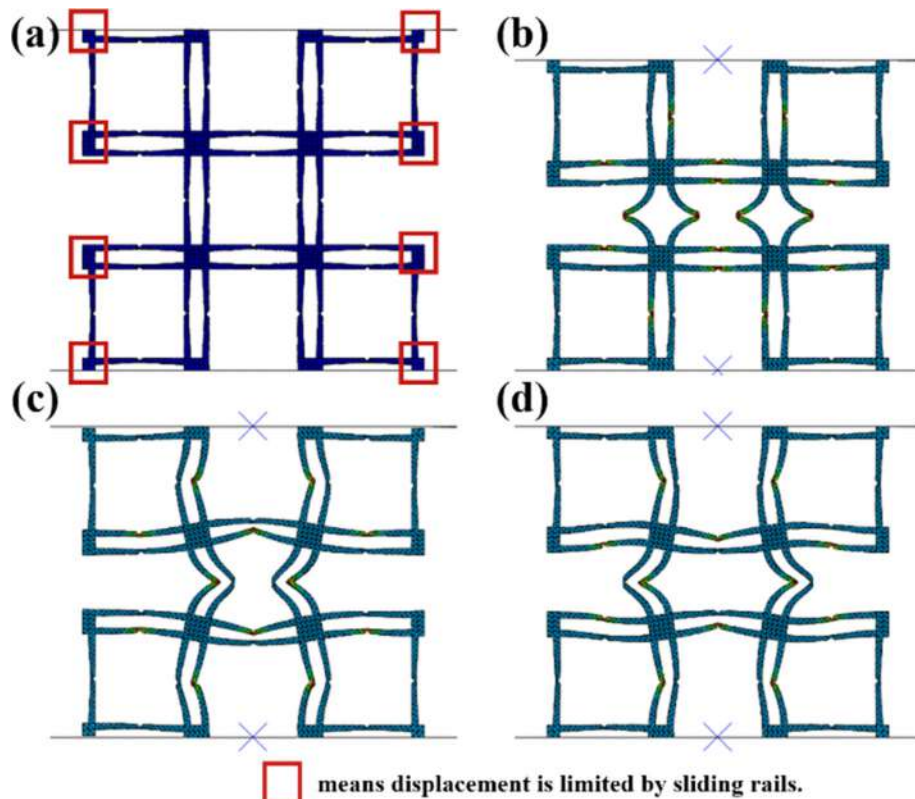

Figure 8. The deformations of different temperature constraints under compression obtained by FE simulation of a cross-shaped five-unit assembly structure, prominent corner points of the outer boundary of the assembly are constrained. (a) Original state, displacement constraints are given. (b) "Twin stars", (c) "X" shape, (d) "Hyperbolic" shape are three different deformations of the assembly under different temperature constraints.

outer boundary of the assembly are constrained. The deformations under compression obtained by FE simulation, shown as Figure 8(b–d), are programmatically controlled by the positions of temperature constraints. Each flexible edge wall can be heated, and the deformation is not constrained by other walls in the same unit or in other units. Considering the independence of the edge walls and the detachability of the unit, the assembly can theoretically achieve any feasible deformation.

Another potential application of this structure is the modulus adjustable structure. As shown in Figure 6(a–b,d), the equivalent modulus of the assembly decreases dramatically when heating the cells of a single layer. In this case, the modulus and deformation sequence of the assembly can be programmed by heating in layers to meet different usage requirements in the field of support, energy absorption, and impact resistance, etc. Such the adjustable mechanism of lattice structure greatly improves its adaptability and potential application fields.

4. Conclusions

In this paper, we proposed a kind of adjustable lattice metamaterials based on the quadrilateral flexible cellular units, and through theoretical, FE simulation and experimental methods, we demonstrated that: The mechanical properties, including the variation relationship between the pressure that increases with strain and the equivalent stiffness that decreases with strain, could be controlled by the material modulus and structural parameters of the units, and the deformation methods, including internal concave, convex and shearing, could be changed due to external temperature and displacement constraints. We demonstrated that: Within a cell, the modulus of the polymer decreases with increasing temperature, and the preferentially deformed heated domains and less-deformed unheated domains are independent of each other. And between the cells, each element is independent of each other regardless of the temperature and displacement constraints. Thus, the intra-cell independence leads to the existence of a sequential order of cell deformation, and the inter-cell independence leads to the modularity of the assembly, the entire assembly is highly programmable as a result. In this way, the metamaterials could be extended to a wider range of applications, such as encoded display and modulus adjustable structure.

5. Experimental section

5.1. Finite element analysis

The commercial FE software Abaqus 2016 was used and the Abaqus/Standard solver was employed for all the simulations. The models were placed between two rigid plates. The temperature constraints were applied to slots, the displacement constraints were applied to prominent corner points and set to $U2 = U3 = 0$, For each position $U3 = 0$. Tetrahedral quadratic element (C3D10MT) with temperature-displacement coupling was used and the modulus

parameter $E_1 = 25.8$ MPa, $E_2 = 1.0$ MPa. The Prony series were obtained from the tensile-relaxation experiment of TPU.

5.2. Construction and assembly

As shown in Figure 7(a), 3D-printed nylon prominent corner points and TPU lattices were linked by metal pins, and the assembly can be disassembled freely through pulling the pins out. To reinforce the units, the edge walls in region ③ (Figures 1(b) and 2(a)) were glue-bonded by the metal sheets to the surface. The bolts inside the corner points can slide up and down in external sliding rails, which were made of acrylic material obtained by laser cutting as Figure 7(c).

5.3. Experiment

Instron testing machine 5944 was used in the compression experiments. Electric heating films were held in slots by clamps as shown in Figure 7(d). The units should be calibrated to the edge lines shown in Figure 7(b) after an experiment was done. To eliminate the residual deformation after the experiment, the structure should be restored to its original shape by restraining the shape through frames and then be placed in hot water.

Disclosure statement

Funding

ORCID

Jinsong Leng 🔟 http://orcid.org/0000-0001-5098-9871

References

[1] L. Yao, R. Niiyama, J. Ou, S. Follmer, C. Della Silva, and H. Ishii, PneUI: pneumatically actuated soft composite materials for shape changing interfaces. In: Proceedings of the 26th Annual ACM Symposium on User Interface Software and Technology, pp. 13–22, 2013.

[2] X. Fang, J. Wen, L. Cheng, D. Yu, H. Zhang, and P. Gumbsch, Programmable gear-based mechanical metamaterials, Nat Mater., vol. 21, no. 8, pp. 869–876, 2022. DOI: 10.1038/s41563-022-01269-3.

[3] X. Yu, J. Zhou, H. Liang, Z. Jiang, and L. Wu, Mechanical metamaterials associated with stiffness, rigidity and compressibility: a brief review, Prog. Mater. Sci. vol. 94, pp. 114–173, 2018. DOI: 10.1016/j.pmatsci.2017.12.003.

[4] J. Huang, J. Zhang, D. Xu, S. Zhang, H. Tong, and N. Xu, From jammed solids to mechanical metamaterials: a brief

review, Curr. Opin. Solid State Mater. Sci., vol. 27, no. 1, pp. 101053, 2023. DOI: 10.1016/j.cossms.2022.101053.

[5] X. Xin, L. Liu, Y. Liu, and J. Leng, 4D Pixel mechanical metamaterials with programmable and reconfigurable properties, Adv. Funct. Mater., vol. 32, no. 6, p. 2107795, 2022. DOI: 10.1002/adfm.202107795.

[6] S. Ankit, Elastic metamaterials and dynamic homogenization: a review, Int. J. Smart Nano Mater., vol. 6, no. 1, pp. 41–60, 2015.

[7] S. Dalela, D.P. Jena, and P.S. Balaji, A review on application of mechanical metamaterials for vibration control, Mech. Adv. Mater. Struct., vol. 29, no. 22, pp. 3237–3262, 2022. DOI: 10.1080/15376494.2021.1892244.

[8] H. Yang, and L. Ma, Design and characterization of axisymmetric auxetic metamaterials, Compos. Struct., vol. 249, pp. 112560, 2020. DOI: 10.1016/j.compstruct.2020.112560.

[9] H. Yin, W. Zhang, L. Zhu, F. Meng, J. Liu, and G. Wen, Review on lattice structures for energy absorption properties, Compos. Struct., vol. 304, no. Part 1, pp. 116397, 2023. DOI: 10.1016/j.compstruct.2022.116397.

[10] M. Yari, and E. Ghavanloo, In-plane elastic properties of metachiral star-shaped lattice structure, Mech. Adv. Mater. Struct., pp. 1–8, 2023. DOI: 10.1080/15376494.2023.2206820.

[11] B.K. Nagesha, V. Dhinakaran, M. Varsha Shree, K.P. Manoj Kumar, D. Chalawadi, and T. Sathish, Review on characterization and impacts of the lattice structure in additive manufacturing, Mater. Today: Proc., vol. 21, no. 1, pp. 916–919, 2020.

[12] M. Gholikord, E. Etemadi, M. Imani, M. Hosseinabadi, and H. Hu, Design and analysis of novel negative stiffness structures with significant energy absorption, Thin. Walled Struct., vol. 181, pp. 110137, 2022. DOI: 10.1016/j.tws.2022.110137.

[13] Q. Li, D. Yang, C. Ren, and X. Mao, A systematic group of multidirectional buckling-based negative stiffness metamaterials, Int. J. Mech. Sci., vol. 232, pp. 107611, 2022. DOI: 10.1016/j.ijmecsci.2022.107611.

[14] Y. Yao, Y. Ni, and L.H. He, Rutile-mimic 3D metamaterials with simultaneously negative Poisson's ratio and negative compressibility, Mater. Des., vol. 200, pp. 109440, 2021. DOI: 10.1016/j.matdes.2020.109440.

[15] S.H. Xiao, C. Zhang, Q.H. Qin, and H. Wang, A novel planar auxetic phononic crystal with periodic cookie-shaped cellular microstructures, Mech. Adv. Mater. Struct., vol. 29, no. 23, pp. 3345–3358, 2022. DOI: 10.1080/15376494.2021.1896057.

[16] H. Yang, B. Wang, and L. Ma, Mechanical properties of 3D double-U auxetic structures, Int. J. Solids Struct., vol. 180-181, pp. 13–29, 2019. DOI: 10.1016/j.ijsolstr.2019.07.007.

[17] M. Wan, K. Yu, and H. Sun, 4D printed programmable auxetic metamaterials with shape memory effects, Compos. Struct., vol. 279, pp. 114791, 2022. DOI: 10.1016/j.compstruct.2021.114791.

[18] A. Montazeri, F. Homafar, and M. Mahnama, A novel 3D compression-torsion mechanical metamaterial with cubic cells based on askew star mechanism: design, simulation, and experimental validations, Mech. Adv. Mater. Struct., pp. 1–10, 2022. DOI: 10.1080/15376494.2022.2150338.

[19] A. Takezawa, and M. Kobashi, Design methodology for porous composites with tunable thermal expansion produced by multimaterial topology optimization and additive manufacturing, Compos. Part B Eng., vol. 131, pp. 21–29, 2017. DOI: 10.1016/j.compositesb.2017.07.054.

[20] S. Kang, W. Liu, H. Song, W. Yuan, C. Qiu, T. Ma, Z. Wang, and J. Wang, Large twist angle of a novel 3D lattice structure via a tailored buckling mode, Mech. Adv. Mater. Struct., pp. 1–12, 2023. DOI: 10.1080/15376494.2023.2180553.

[21] J. Mueller, J.A. Lewis, and K. Bertoldi, Architected Multi-material Lattices with Thermally Programmable Mechanical Response, Adv Funct Mater., vol. 32, no. 1, pp. 2105128, 2022. DOI: 10.1002/adfm.202105128.

[22] T. Chen, M. Pauly, and P.M. Reis, A reprogrammable mechanical metamaterial with stable memory, Nature., vol. 589, no. 7842, pp. 386–390, 2021. DOI: 10.1038/s41586-020-03123-5.

[23] U. Sajjad, T. Rehman, M. Ali, C.W. Park, and W.M. Yan, Manufacturing and potential applications of lattice structures in thermal systems: a comprehensive review of recent advances, Int. J. Heat Mass Transf., vol. 198, pp. 123352, 2022. DOI: 10.1016/j.ijheatmasstransfer.2022.123352.

[24] J. Feng, B. Liu, Z. Lin, and J. Fu, Isotropic octet-truss lattice structure design and anisotropy control strategies for implant application, Mater. Des., vol. 203, p. 109595, 2021. DOI: 10.1016/j.matdes.2021.109595.

[25] C. Pan, Y. Han, and J. Lu, Design and optimization of lattice structures: a review, Appl. Sci., vol. 10, no. 18, pp. 6374, 2020. DOI: 10.3390/app10186374.

[26] J. Liu, and Y. Zhang, Soft network materials with isotropic negative Poisson's ratios over large strains, Soft Matter., vol. 14, no. 5, pp. 693–703, 2018. DOI: 10.1039/c7sm02052j.

[27] M. Zarek, M. Layani, I. Cooperstein, E. Sachyani, D. Cohn, and S. Magdassi, 3D Printing of shape memory polymers for flexible electronic devices, Adv Mater., vol. 28, no. 22, pp. 4449–4454, 2016. DOI: 10.1002/adma.201503132.

[28] A. Clausen, F. Wang, J.S. Jensen, O. Sigmund, and J.A. Lewis, Topology optimized architectures with programmable poisson's ratio over large deformations, Adv Mater., vol. 27, no. 37, pp. 5523–5527, 2015. DOI: 10.1002/adma.201502485.

[29] S.C. Joshi, and A.A. Sheikh, 3D printing in aerospace and its long-term sustainability, Virtual Phys. Prototyping., vol. 10, no. 4, pp. 175–185, 2015. DOI: 10.1080/17452759.2015.1111519.

[30] C. Wang, Y. Li, W. Zhao, S. Zou, G. Zhou, and Y. Wang, Structure design and multi-objective optimization of a novel crash box based on biomimetic structure, Int. J. Mech. Sci., vol. 138–139, pp. 489–501, 2018. DOI: 10.1016/j.ijmecsci.2018.01.032.

[31] A. Sorrentino, and D. Castagnetti, Negative Poisson's ratio lattice for designing vertebral biomaterials, Mech. Adv. Mater. Struct., vol. 29, no. 27, pp. 6626–6633, 2022. DOI: 10.1080/15376494.2021.1983089.

[32] S.F. Khosroshahi, S.A. Tsampas, and U. Galvanetto, Feasibility study on the use of a hierarchical lattice architecture for helmet liners, Mater Today Commun., vol. 14, pp. 312–323, 2018. DOI: 10.1016/j.mtcomm.2018.02.002.

[33] Y. Gao, X. Wei, X. Han, Z. Zhou, and J. Xiong, Novel 3D auxetic lattice structures developed based on the rotating rigid mechanism, Int. J. Solids Struct., vol. 233, pp. 111232, 2021. DOI: 10.1016/j.ijsolstr.2021.111232.

[34] B. Fan, Z. Xu, Y. Lin, and Z. Huang, Mechanical properties of a novel two-phase hybrid plate-lattice metamaterial, Mech. Adv. Mater. Struct., vol. 30, no. 23, pp. 4752–4763, 2023. DOI: 10.1080/15376494.2022.2104974.

[35] J. Ou, M. Zhao, P. Jannik, S. Dai, V. Nikolaos, and I. Hiroshi, KinetiX - designing auxetic-inspired deformable material structures, Comput. Graph., vol. 75, pp. 72–81, 2018. DOI: 10.1016/j.cag.2018.06.003.

[36] Z. Huang, B. Li, L. Ma, and Y. Li, Mechanical properties and energy absorption performance of bio-inspired dual architecture phase lattice structures, Mech. Adv. Mater. Struct., vol. 30, no. 9, pp. 1842–1852, 2023. DOI: 10.1080/15376494.2022.2045654.

[37] W. Zhang, L. Qin, J. Wang, and W. Xu, A pixel design method for mechanical metamaterials based on topology optimization, Mech. Adv. Mater. Struct., pp. 1–9, November 2022. DOI: 10.1080/15376494.2022.2142711.

[38] Z. Meng, M. Liu, H. Yan, G.M. Genin, and C.Q. Chen, Deployable mechanical metamaterials with multistep programmable transformation, Sci. Adv., vol. 8, no. 23, pp. eabn5460, 2022. DOI: 10.1126/sciadv.abn5460.

Appendix A: Material property test

For the TPU material, the appropriate dog bone shaped specimen was 3D printed according to ASTM D638 Type IV, and $25 \times 19 \times 3$ mm aluminum reinforcing sheets with $45°$ chamfers were attached to the
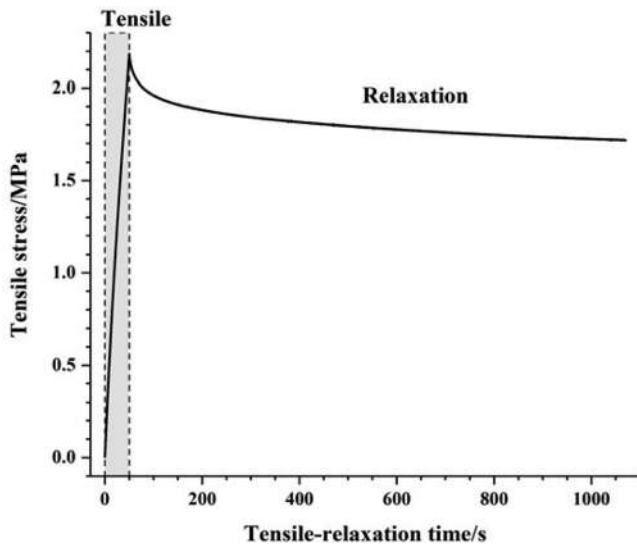
Figure A.1. The stress-time curve of the tensile-relaxation process for TPU specimen.

Table A.1. The values of Prony series obtained by relaxation test.

Term	Series g_i	Series k_i	Relaxation time τ_i^g
1	0	0	0.1
2	0	0	1
3	0.14516	0	10
4	0.17267	0	100
5	0.07649	0	1000
∞	0.60568	1	–

top and bottom of each end. Instron 5944 tensile tester was used for the room temperature tensile-relaxation test, with the tensile rate of the tester set at 0.1 mm/s and the tensile deformation set at 5 mm for 50 s. Then the current 5 mm tensile deformation was maintained for 1000s. The stress-time curve of the tensile-relaxation process at the central position of the specimen was obtained, given in Figure A.1.

From the stress-time curve obtained by the relaxation test, the variation of the energy storage modulus with time can be determined. It can be converted into kernel functions. By exponential fit, the Prony series and the normalized residual modulus at each relaxation time can be obtained. The values obtained for Prony series are shown in Table A.1.